Operando Elucidation of Electrocatalytic and Redox Mechanisms on a 2D Metal Organic Framework Catalyst for Efficient Electrosynthesis of Hydrogen Peroxide in Neutral Media

R. Dominic Ross,[1] *Hongyuan Sheng,*[1] *Yujia Ding,*[2] *Aurora N. Janes,*[1] *Dawei Feng,*[1,3] *JR Schmidt,*[1] *Carlo U. Segre,*[2] *and Song Jin*[*,1]

[1]Department of Chemistry, University of Wisconsin–Madison, 1101 University Avenue, Madison, Wisconsin 53706, United States

[2]Department of Physics and CSRRI, Illinois Institute of Technology, Chicago, Illinois 60616, United States

[3]Department of Materials Science and Engineering, University of Wisconsin-Madison, Madison, Wisconsin 53706, United States

ABSTRACT

Practical electrosynthesis of hydrogen peroxide (H_2O_2) is hindered by the lack of inexpensive and efficient catalysts for the two-electron oxygen reduction reaction ($2e^-$ ORR) in neutral electrolytes. Here, we show that Ni_3HAB_2 (HAB = hexaaminobenzene), a two-dimensional metal organic framework (MOF), is a selective and active $2e^-$ ORR catalyst in buffered neutral electrolytes with a linker-based redox feature that dynamically affects the ORR behaviors. Rotating ring-disk electrode measurements reveal that Ni_3HAB_2 has high selectivity for $2e^-$ ORR (>80% at 0.6 V vs. RHE) but lower Faradaic efficiency due to this linker redox process. Operando X-ray absorption spectroscopy measurements reveal that under argon gas the charging of the organic linkers causes a dynamic Ni oxidation state, but in O_2-saturated conditions the electronic and physical structure of Ni_3HAB_2 change little and oxygen-containing species strongly adsorb at potentials more cathodic than the reduction potential of the organic linker (E_{redox} ~ 0.3 V vs. RHE). We hypothesize that a primary $2e^-$ ORR mechanism occurs directly on the organic linkers (rather than the Ni) when $E > E_{redox}$, but when $E < E_{redox}$, H_2O_2 production can also occur through Ni-mediated linker discharge. By operating the bulk electrosynthesis at a low overpotential (0.4 V vs. RHE) up to 662 ppm of H_2O_2 can be produced in a buffered neutral solution in an H-cell due to minimized strong adsorption of oxygenates. This work demonstrates the potential of conductive MOF catalysts for $2e^-$ ORR and the importance of understanding catalytic active sites under electrochemical operation.

KEYWORDS: oxygen reduction reaction; selective electrocatalysis; metal organic framework; hydrogen peroxide, operando; X-ray absorption spectroscopy

INTRODUCTION

Hydrogen peroxide (H_2O_2) is a powerful oxidant and disinfectant with broad industrial, environmental and household applications. Its annual production exceeds 5 million tons, and is projected to continue to grow steadily.[1,2,3] To date, much of the world's H_2O_2 has been produced by the centralized anthraquinone process, which requires energy intensive distillation steps and metal catalysts to produce highly concentrated (>70 wt%) H_2O_2 that is then typically diluted to concentrations as low as 0.1 wt% for use.[4] The prevalent applications of these dilute H_2O_2 solutions make the hazard of H_2O_2 transport from centralized production locations an unnecessary risk. Electrosynthesis of H_2O_2 via the two-electron oxygen reduction reaction ($2e^-$ ORR) presents a promising alternative that could be cheaper and safer than the prevailing anthraquinone process.[5] Particularly, if H_2O_2 could be electrosynthesized in neutral solutions, H_2O_2 could be stored due to better stability (compared to alkaline solutions[6]) and directly utilized at the point of use.

To realize practical H_2O_2 electrosynthesis in neutral solutions, inexpensive earth-abundant catalysts with high activity and selectivity towards $2e^-$ ORR (as opposed to the four-electron ORR process that produces H_2O) are required. To date, very few active $2e^-$ ORR catalysts in neutral media have been reported, and only a few demonstrations of practical electrosynthesis of H_2O_2 in neutral conditions exist.[7,8] Additionally, most reports of neutral $2e^-$ ORR do not use buffered electrolytes for neutral conditions,[9,10] so proton consumption at the electrode can cause shifts towards alkaline pH, in which H_2O_2 is unstable.[6] Therefore, the intrinsic activity at neutral pH could be inaccurately represented. Single-atom-catalysts (SACs) have emerged as promising $2e^-$ ORR catalysts,[9,11–13] but the difficulty of characterizing their catalytic active structures hinders their developement[14] because these $2e^-$ ORR SAC catalysts are highly sensitive to the electronic structure of adjacent atomic sites.[11,15] Therefore, it is desirable to control the catalytic active site

environments to systematically improve their design for optimized $2e^-$ ORR activity and selectivity. Tunability could be achieved in metal chalcogenide catalysts with well-defined crystal structures,[8,16–20] but these compounds are primarily active in acidic media and sometimes require further post-treatment to improve stability[16] and minimize hazardous metal leaching.

In this context, metal organic frameworks (MOFs) are appealing for $2e^-$ ORR catalysis because their periodic and highly tunable structures allow their active site environments to be specifically tailored towards high activity and selectivity.[21–23] The porous structures of MOFs and variety of available organic linkers[24] allow for intrinsically high electrochemically active surface area and tunable mass-transport to the active sites.[25] The recent developments of two-dimensional (2D) MOFs that have intrinsically high electrical conductivity and tunable electronic structures via controlling the composition of the metal sites[22,26,27] make MOFs promising electrocatalysts. These structurally well-defined MOF catalysts are more readily characterized to reveal important structural features contributing to $2e^-$ ORR selectivity, in contrast to the difficulty of systemically establishing the contributions of these features in SACs.[14] Furthermore, SACs that have been reported as active and selective $2e^-$ ORR catalysts contain the square-planar coordinated M-N_4 motif, where the M (with the highest performance) is typically Co or Ni,[11,12,14] motifs that are also found in 2D MOFs. Specifically, two families of 2D MOFs containing the M-N_4 motif, M_3HITP_2 ("M-HITP", HITP = hexaiminotriphenylene)[28] and M_3HAB_2 ("M-HAB", HAB = hexaaminobenzene, M = Co, Ni, Cu)[29–32] have recently been identified as $2e^-$ ORR catalysts computationally[33–35] and experimentally in alkaline media.[36,37]

The drastic differences in ORR activity between MOFs with different metal nodes[37–40] in alkaline media have led to questions about the nature of the active site on these M-N_4 MOFs. While several M-N_4 SACs have been shown experimentally to have metal active sites, computational

studies on both Ni-HITP[35] and Ni-HAB[37] suggest that the organic linkers could contain the active sites. Ni-HAB in particular has been noted for its intrinsic redox activity[32,41] and ambipolar behaviors between inert and ambient environments.[31] Furthermore, other MOF systems have been demonstrated to have highly redox-dependent O_2-adsorption energies[42] suggesting unexplored consequences on Ni-HAB's ORR mechanism. Nonetheless, Ni-HAB's potential as a $2e^-$ ORR catalyst towards H_2O_2 electrosynthesis in the more practical neutral solutions has not been demonstrated and its operating active site environment has not been characterized and understood to date. In situ or operando synchrotron X-ray absorption spectroscopy (XAS) is a powerful technique for characterization of the operating environments of M-N_4 catalysts,[43,44] because it can be adsorbate sensitive and give coupled local structure and bulk electronic structure information.[45,46] Here, we show Ni-HAB's excellent intrinsic selectivity towards $2e^-$ ORR in neutral conditions, study the details of its operating active site environments using operando XAS, propose the catalytic mechanisms entangled with the redox feature of the organic linker, and demonstrate the practical electrosynthesis of H_2O_2 in a bufferred neutral solution.

RESULTS AND DISCUSSION

Synthesis and Characterization of Ni-HAB Powder. The Ni-HAB catalyst (Figure 1a) was prepared according to previously reported procedures,[37] wherein the HAB linker and Ni nitrate were reacted in water in the presence of a base (see Supporting Information for experimental details). Because the presence of O_2 heavily influences the growth[47] (Figure S1), the Ni-HAB catalyst was also prepared in air to obtain the high surface area nanostructured powder suitable for electrocatalysis. The dependence of crystallite size on the oxygen diffusion rate suggests that HAB can be spontaneously oxidized in air, which then facilitates its coordination to Ni. Since HAB initially becomes partially deprotonated in base and then subsequently loses three hydrogens and

three electrons via the chemical oxidation by O_2,[32] the linker coordinated by Ni in the Ni-HAB exists in a fundamentally different oxidation state than the free HAB linker. Scanning electron microscopy (SEM) image (Figure 1b) reveals the nanoscale morphology of Ni-HAB catalyst with high surface area, which is quantitatively confirmed by Brunauer-Emmett-Teller (BET) analysis (Figure S2).

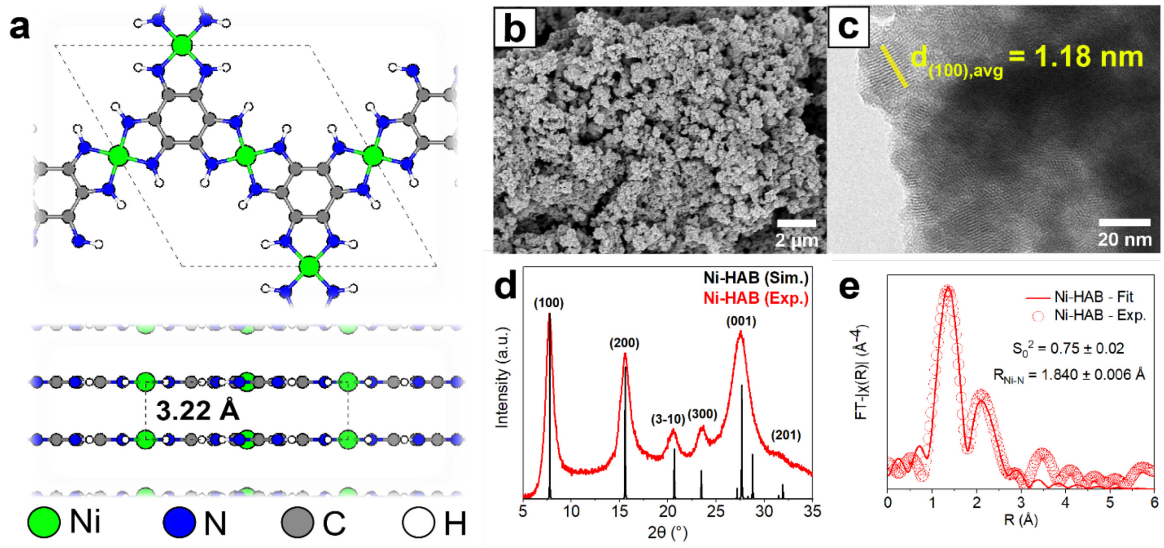

Figure 1. Crystal structure and structural characterization of Ni_3HAB_2. a) Crystal structure of Ni-HAB viewed along the *c*-axis (top) and the *a*-axis (bottom). b) SEM image of nanoscale Ni-HAB powder. c) TEM micrograph of dispersed Ni-HAB with experimentally measured (100) plane spacing labeled. d) PXRD pattern of Ni-HAB (red) in comparison with the simulated pattern (black). e) EXAFS and fitting of Ni-HAB powder with Ni-N bond distances and S_0^2 obtained by the fitting.

Transmission electron microscopy (TEM) shows the periodic structure of the catalyst (Figure 1c) with an observed average distance of 1.18 nm between (100) planes that agrees with the expected (100) plane spacing of 1.20 nm. The powder X-ray diffraction (PXRD) pattern (Figure 1d and Figure S3) also confirms the crystallinity along other planes, and the agreement

between experimental peaks and the PXRD pattern simulated from the Ni-HAB crystal structure confirms the phase purity. The Raman spectrum of the powder (Figure S4) is consistent with previous reports.[36,37] Finally, X-ray absorption spectroscopy (XAS) conducted at Beamline 10-BM of the Advanced Photon Source[48] was used to obtain the extended X-ray absorption fine structure (EXAFS) Ni K-edge spectrum of Ni-HAB (Figure 1e), which shows a similar spectrum to literature.[49] The ensemble averages of Ni-N and Ni-C bond distances derived from the fitting of the Ni-HAB EXAFS using the standard Ni-HAB structure as a model (see Supporting Information for details) agree reasonably well with those from the reported crystal structure (Table S1). From this fitting (using fixed coordination numbers from the crystal structure) we also obtained a value of 0.75 ± 0.02 for the amplitude reduction factor (S_0^2) which was used to determine the coordination changes in subsequent fittings.

Rotating Ring Disk Electrode Measurements of Ni-HAB Electrocatalyst. We used a rotating ring-disk electrode (RRDE) to evaluate the activity and selectivity of Ni-HAB towards $2e^-$ ORR (see Supporting Information for details). From a typical linear sweep voltammetry (LSV) scan from 0.8 V to 0 V vs. RHE (before *iR* correction), the H_2O_2 selectivity appears to peak at ~50% and then drop rapidly (Figure 2, dashed black line). However, the ring current is consistently ~1 mA/cm^2_{disk} across the potential range, which is especially high considering the low catalyst loading used (equivalent to 83 $\mu g_{Ni}/cm^2_{disk}$, 79 $\mu g_N/cm^2_{disk}$, 68 $\mu g_C/cm^2_{disk}$). When the catalyst is instead measured using RRDE and a series of brief chronoamperometry (CA) steps (Figure 2 red dots and Figure S5), the ring current remains consistent, but the apparent selectivity drastically increases at less cathodic potentials due to a large decrease in the overall current observed at the disk. This suggests that minimizing charging current during measurement leads to an apparently "higher" selectivity. Importantly, by measuring the current in an Ar-saturated solution (Figure 2 blue line,

more details in Figure S6) it becomes evident that most of the reductive current at the disk occurs independent of the ORR. Furthermore, when the Ar-saturated LSV current is subtracted from the O_2-saturated LSV current at the disk, a similar selectivity profile to that of the CA measurement is obtained (Figure S6). *Thus, much of the observed disk current might be due to the MOF's intrinsic redox feature, which has been previously observed and hypothesized to take place via reduction of the organic linker.*[37,41]

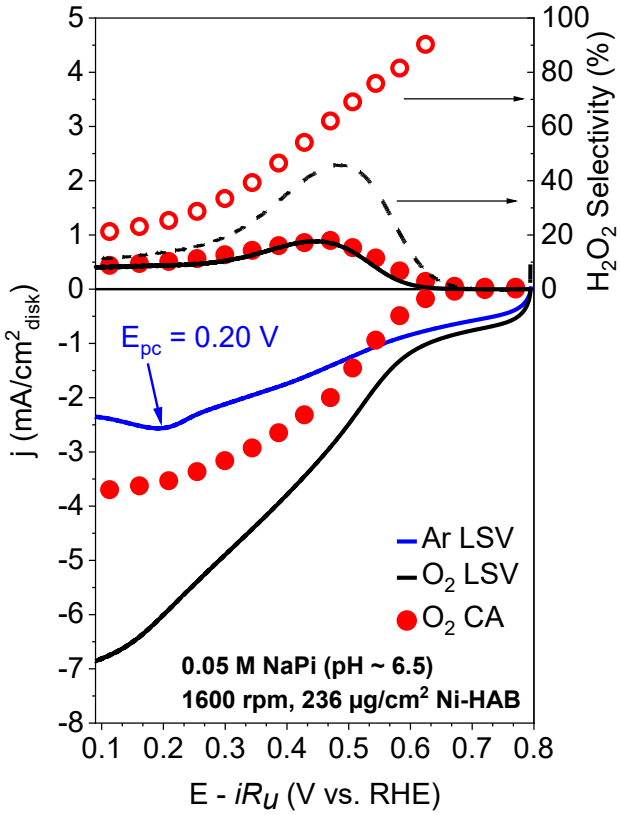

Figure 2. RRDE voltammograms of Ni-HAB measured at 1600 rpm in O_2-saturated or Ar-satured 0.05 M NaPi buffer solution (pH = 6.5-6.6) measured by either linear sweep voltammetry at 50 mV/s (black lines: O_2 saturation, blue line: Ar saturation) or chronoamperometry (red dots); and their corresponding H_2O_2 selectivity (dashed line and open circles).

Cyclic voltammetry (CV) on the Ni-HAB catalyst in an Ar-saturated environment shows that the half-wave potential of this redox event of the linker (from now on referred to as E_{redox}) is 0.29 V vs. RHE (Figure S7a and b), which further validates a linker based redox process, since a Ni based redox would likely occur at a much more anodic potential.[50] Due to the coordination with Ni and the changes to HAB's redox state during the growth process, the linker redox behavior in Ni-HAB is fundamentally different from the behaviors of the free HAB linker (Figure S7c and d). There is also a change in the slope in the Ar-subtracted LSV near this potential (Figure S6), suggesting that this linker redox event may actually change the mechanism of the ORR. Moreover, the LSV measured in Ar (Figure 2 blue line) shows a clear decrease in current density at 0.20 V, which we will refer to as E_{pc}. At this potential, which is also the cathodic peak potential in the CV shown in Figure S7, most of the organic linker is reduced in Ar. In contrast, the LSV measured in O_2 (mix of ORR and redox current) shows much larger current than the LSV measured in Ar (only redox current) or the CA points measured in O_2 (mix of ORR and lower redox current) and does not show a decrease when $E < E_{pc}$. This further suggests that ORR and the linker redox processes do not have additive behavior, but rather some interaction. Regardless of the method used for the selectivity measurement, a severe drop in H_2O_2 selectivity was observed when $E < E_{redox}$ (or approaching E_{redox}), where the redox activity becomes prevelant.

To put Ni-HAB's catalytic performance in neutral electrolyte into context, we also synthesized Cu-HAB with a directly analogous structure to Ni-HAB and Ni-HITP with a similar $Ni-N_4$ structural motif to Ni-HAB (see details in Supporting Information, PXRD shown in Figure S3) and measured their catalytic performance as a comparison, to study the influence of the M-HAB catalyst metal node on the $2e^-$ ORR activity and compare to Ni-HITP's previous promising selectivity in alkaline electrolyte.[28,40] Cu-HAB exhibits low catalytic activity and selectivity

towards $2e^-$ ORR in neutral condition(Figure S8). Ni-HAB is significantly more selective and active towards $2e^-$ ORR in neutral condition at lower overpotentials compared to Ni-HITP (Figure S8). At high overpotentials, the selectivity of Ni-HITP does increase but the overall ring current remains low, therefore the overall produced H_2O_2 remains lower for Ni-HITP. Such differences could be due to the superior nanoconfinement in the eclipsed π-π stacking and small 0.8 nm pores of the Ni-HAB structure, as opposed to the slipped parallel stacking structure and larger 2 nm pores of Ni-HITP.[28,32] Nanoconfinement has been previously demonstrated to be a powerful strategy towards tuning higher selectivity in Ni-N_4 catalysts.[51,52]

Operando X-ray Absorption Spectroscopy of Ni-HAB to Probe Redox and Electrocatalytic mechanisms. To explore the relationship between the redox activity of Ni-HAB and its ORR catalytic activity, we conducted operando X-ray absorption spectroscopy (XAS) studies of the catalyst at the Ni K-edge at Beamline 10-ID of the Advanced Photon Source.[53] To separate the effects of the Ni-HAB redox and the effects of the ORR on Ni-HAB, we subjected two identical Ni-HAB electrodes to the same set of electrochemical conditions, where one was measured in O_2-saturated electrolyte and the other was measured in Ar-saturated electrolyte. We employed a custom-built electrochemical H-cell for fluorescence XAS (Figure S9) with a working electrode consisting of Ni-HAB powder dropcast onto carbon fiber paper (CFP), here referred to as Ni-HAB/CFP. The catalyst's Ni K-edge was continuously monitored by XAS when the electrode was held at a series of constant potentials for 75 minutes each (Figure 3a and Figure S10, see Supporting Information for details). The ratio of current observed under the two gas conditions is similar to that observed in RRDE (see Figure 2).

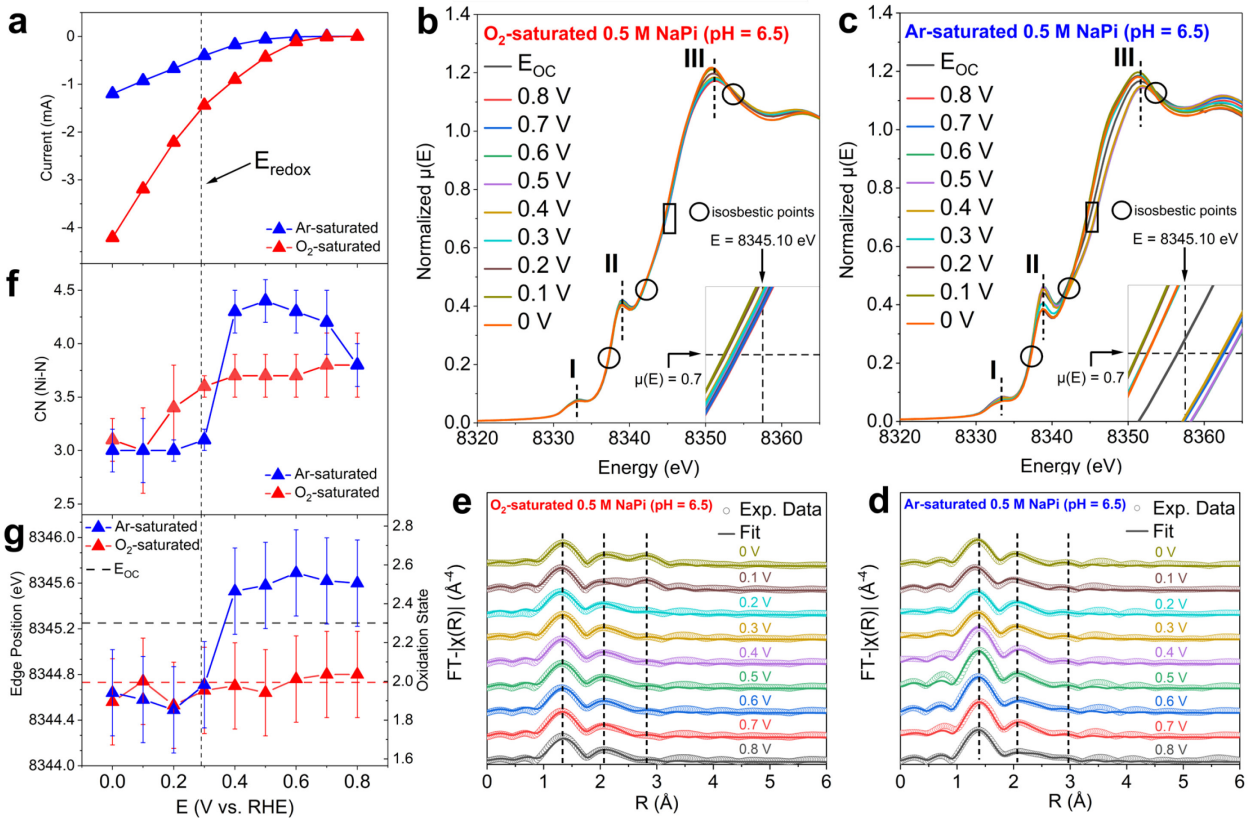

Figure 3. Operando XAS study of the ORR catalytic process on Ni-HAB/CFP. a) Current for each constant applied potential on Ni-HAB/CFP after 1 hour 15 minutes. XANES of Ni-HAB/CFP at various applied potentials in b) O_2-saturated and c) Ar-saturated electrolyte, and the corresponding EXAFS of Ni-HAB/CFP under d) Ar-saturation and e) O_2-saturation at different cathodic potentials. f) The extracted EXAFS coordination numbers for Ni-HAB/CFP under O_2 and Ar-saturation, and g) the extracted XANES Ni K-edge positions for Ni-HAB/CFP under O_2 and Ar-saturation. The open circuit potential before applied potential is labeled as E_{OC} in panel b and c. The vertical line in panel a, f, g marks the half-wave redox potential (E_{redox}).

The X-ray absorption near edge spectroscopy (XANES) for the Ni-HAB samples under both the O_2-saturated condition (Figure 3b) and Ar-saturated condition (Figure 3c) show pre-edge peaks that correspond to the 1s-3d transition at ~8333 eV (peak I) and 1s-4p_z transition at ~8339

eV (peak II) which are consistent with a square-planar Ni complex.[41,54,55] The consistent peak I and II during ORR operation (Figure 3b) confirm that the Ni nodes maintain their initial +2 oxidation state and square-planar geometry, which is further supported by the lack of significant shift in the edge energy relative to the edge position measured at the open circuit potential before any potential was applied (E_{OC}). Furthermore, the edge position appears independent of the potential, which suggests that Ni is not the active site for ORR. This behavior is consistent with a previous study that conducted potential stepping under an ambient environment.[41]

In contrast to the O_2-saturated condition, under Ar-saturation the Ni sites appear to have a highly dynamic oxidation state under cathodic potentials (Figure 3c). Given the more oxidizing environment due to the presence of O_2 (and the production of H_2O_2 under applied potential) it was expected that O_2-saturation would have more oxidized Ni sites (corresponding to a higher Ni K-edge energy). Surprisingly, the Ni K-edge position at E_{OC} under Ar-saturation is higher than any of the edge positions in the O_2-saturated condition. Under applied potentials anodic to the redox potential (i.e. $E > E_{redox}$ ~0.3 V vs. RHE), the edge position shifts even higher, suggesting an oxidation around the Ni site, likely as a result shifting charge density as the adjacent N sites on the linker are oxidized under the anodic applied potential. Then, when $E \leq E_{redox}$, Ni becomes more reduced than the E_{OC} resting state, and the edge position becomes similar to that observed under O_2-saturation. This suggests that in the O_2-saturated environment, Ni intrinsically stays in its reduced state, while in Ar-saturated electrolyte the oxidation state of Ni cycles with the cycling of the HAB linker. However, the open circuit potentials shift cathodically under both gas conditions (Figure S11), which suggests similar electronic modification occurs at the linker in both conditions. A previous study[31] suggested the p-type conduction of Ni-HAB in air could be a result of ambient O_2-adsorption creating mobile holes in the linker, which could work to maintain a

balance of oxidized HAB (HAB_{ox}) and reduced HAB (HAB_{red}). The partial oxidation of some of these linkers to maintain this balance could create reduced oxygen species, or these unexpected reduced oxidation states under O_2-saturation could be a result of geometric distortions around Ni. On the other hand, under Ar-saturated conditions Ni becomes oxidized as the HAB linker becomes oxidized by applying $E > E_{redox}$, as charge density shifts between Ni and the linker. When $E < E_{redox}$, Ni returns to its native +2 oxidation state as HAB is reduced and charge transfer occurs between the linker and Ni. Due to this charge delocalization through the MOF, the Ni XANES in Ar serves as an indirect probe of the linker redox.

To further understand the differences between O_2-saturated and Ar-saturated environments during the electrochemical operation of Ni-HAB, we examined the extended X-ray absorption fine structure (EXAFS) and used the DFT optimized crystal structures of Ni-HAB to fit the data up to 3 Å (Figure 3d, e, and see Supporting Information for details, Figure S12-S18, Tables S2-S19). The first two major peaks in the EXAFS under O_2-saturation showed very little changes in position or intensity (Figure 3e), suggesting that local structural degradation does not occur on the timescale of the experiment. The structural stability of the surface was further confirmed by the lack of changes observed in operando Raman spectroscopy (Figure S19). However, there is a noticeable uplift at ~3 Å at more cathodic potentials ($\leq$ 0.2 V) (Figure 3e), which is tentatively assigned to an oxygen adsorbate, based on approximate Ni-O bond distances of DFT predicted structures of *OOH adsorbed on the linker sites of Ni-HAB (Figure S20-S21, Table S20). The DFT predicted structures were used as starting models to fit the O_2-saturated EXAFS data at high potentials where the adsorbates are observed. Furthermore, strongly adsorbed *OOH at high potentials was previously observed for $CoSe_2$,[20] where an uplift of the XANES whiteline corresponded to the strong adsorption of *OOH, similar to the uplift observed in the O_2-saturated XANES at potentials

≤ 0.2 V (Figure 3b). Oxygen-based adsorbates have been previously integrated into EXAFS fittings of ORR on SACs by a similar trial-and-error approach.[43] Notably, the fitting results for the Ar-saturated EXAFS did not have the appearance of such a path at highly cathodic potentials, but instead showed a changing intensity and systematic contraction of the Ni-N first-shell path (Figure 3d). This further supports the hypothesis that the uplift of the new ~3 Å path in the O_2-saturated EXAFS results from an oxygenate adsorbate. Even though there is also a small peak at ~3 Å in the Ar-saturated EXAFS (observed value of 2.91 Å at 0 V vs. RHE, see Figure S18), its intensity does not change and it is clearly shifted by 0.12 Å at 0 V vs. RHE from the position of the peak observed in the O_2-saturated EXAFS (2.79 Å at 0 V vs. RHE, see Figure S14), clearly indicating that it intrinsically originates from the Ni-HAB structure. The Ni-N (R_{eff} = 1.838 Å), Ni-C (R_{eff} = 2.687 Å) and Ni-N-C (R_{eff} = 2.932 Å) scattering paths all have predicted minor peaks at ~2.9 Å, further validating the potential-independent peak observed in the Ar-saturated and ($E > E_{redox}$ O_2-saturated EXAFS) spectra as originating from Ni-HAB, but the uplift and shift are indicative of a distinct potential-dependent peak that could not originate from Ni-HAB without other large structural perturbations. Linear combination analysis (LCA) fitting using the XANES spectrum for 0.8 V vs. RHE in Ar-saturated electrolyte as a standard for 100% HAB_{ox} and the XANES spectrum for the 0 V vs. RHE in Ar-saturated electrolyte as a standard for 100% HAB_{red} (Figure S22) confirms that the speciation crossover corresponds to the red shift of the edge energy, and that the oxygenate adsorbates become observable in EXAFS when the speciation is 100% HAB_{red} (for Ar-saturated electrolyte). The crossover point of the HAB_{red} and HAB_{ox} fractions (0.34 V vs. RHE) is also close to the E_{redox} (0.29 V vs. RHE). Additionally, LCA reveals that the primary speciation in an O_2-saturated environment is HAB_{red}, and further reaches 100% HAB_{red} at potentials ≤ 0.2 V vs. RHE. The initially high fraction of HAB_{red} in the O_2 saturated XANES is strange, and could suggest

some limitation of Ni K-edge XANES as an oxidation state probe[56] in such a complex chemical environment.

We further quantitatively extracted the Ni coordination numbers from both sets of EXAFS fittings using the amplitude reduction factor determined from the powder fittings (Figure 3f). At 0.8 V vs. RHE, Ni shows similar coordination under the O_2-saturated and Ar-saturated environments, which is consistent with the ideal square planar four-coordinated Ni. As the potential is swept from 0.8 V to 0 V vs. RHE, a sharp drop in coordination is observed for Ni-HAB under Ar-saturation between 0.4 V and 0.3 V vs. RHE. The large drop is attributed to the reduction of the linker, essentially reversing the linker oxidation process that initially allows the coordination to Ni during the Ni-HAB synthesis. Under O_2-saturation, the coordination remains mostly consistent until 0.3 V vs. RHE, after which the coordination consistently drops. This drop in coordination is likely due to the presence of the strongly adsorbed oxygenate species on the Ni site disrupting the bonding to the reduced linkers, which is also predicted by DFT calculations (Figure S20-21). This bonding disruption could be one cause of Ni leaching into solution (Figure S23), which is more severe in Ar-saturated electrolyte than in O_2-saturated electrolyte. Using an estimate of 1.7 eV/oxidation state for Ni K-edge XANES for Ni oxides based on previous studies,[57,58] we summarize the XANES data and assess the oxidation states of the Ni sites during electrochemical operation in Figure 3g (see Supporting Information for details). Interestingly, the trend of the Ni K-edge position vs. potential appears quite similar to the trend of the first-shell coordination number vs. potential for Ni-HAB in the Ar-saturated environment. The full results of all fittings are shown in Tables S1-S19.

Mechanisms of ORR on Ni-HAB. To further investigate the adsorption of oxygen-containing species on Ni-HAB at higher overpotentials ($E < E_{redox} \sim 0.3$ V vs. RHE), we collected the EXAFS

spectra after the cathodic CA measurements while allowing the electrode to rest in solution at E_{OC} (Figure 4a and Figure S24). The major path assigned to oxygen scattering (Ni-$O_{ads,C/N}$) at ~2.8 Å showed a small decrease after the measurement, and appeared to completely disappear once the solution was taken out of the electrolyte and dried. Accordingly, the minor oxygen scattering path (Ni-H/C/$O_{ads,Ni}$) appeared to increase back to closer to the original relative intensity of the sample. These results suggest that some of the adsorbed oxygen-containing species are released when the high cathodic potential is no longer applied, and the adsorbate becomes unstable out of solution. However, the adsorbate binding behavior is clearly modified by the redox process, as evidenced by the initially persistent surface intermediate observed in the EXAFS after the potential is "turned off," as a result of the stronger surface binding to the redox modified catalyst. The large disk scan rate dependent peaks in the ring current after cathodic LSV sweeps of Ni-HAB on an RRDE after turning off the applied potential at the disk (Figure 4b) reveal adsorbed H_2O_2 to be the dominant adsorbate at high potentials. The increase in the ring current (increased total H_2O_2 production) and the shifting of the peak to longer times after the disk shutoff suggests that when higher potentials are scanned for longer periods of time, more H_2O_2 is produced at the electrode and subsequently released over a short time period.

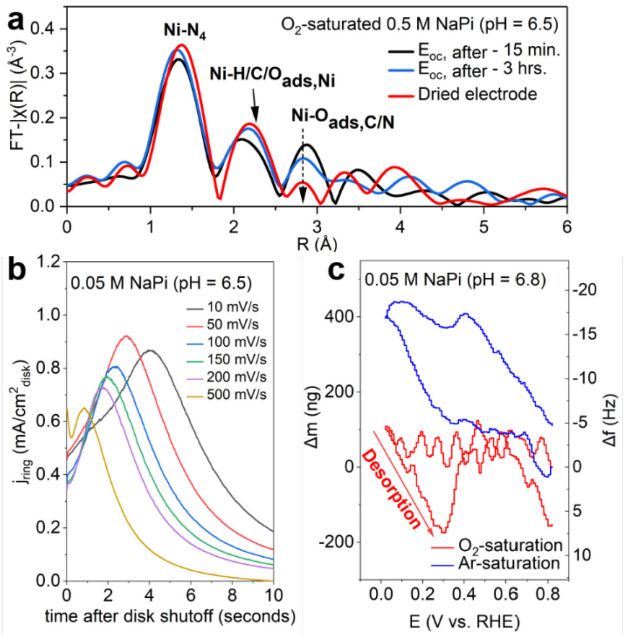

Figure 4. Investigation of adsorbate species on Ni-HAB. a) Ni K-edge EXAFS of Ni-HAB after ORR scans, b) time dependence of the RRDE ring current (held at 1.3 V vs. RHE) after ORR scans, and c) mass changes of the Ni-HAB during electrochemical cycling under different gas environments measured by EQCM.

We further carried out electrochemical quartz crystal microbalance (EQCM) measurements of the Ni-HAB during electrochemical cycling (see Supporting Information and Figure S25 for details) under both Ar-saturation and O_2-saturation (Figure 4c, Figure S26). Under Ar-saturation, mass increases steadily during the cathodic sweep and starts increasing more rapidly when $E < E_{redox}$ (~ 0.3 V vs. RHE) of Ni-HAB. In the oxidative sweep, the behavior is semi-reversible but results in a ~100 ng mass increase at the beginning of the cycle, reflecting the only quasi-reversible proton-coupled redox process of the linker. In contrast, under O_2-saturation, only a slight initial mass increase is observed during the cathodic sweep with the rest staying mostly flat, and then on the oxidative sweep a notable mass decrease that peaks at 0.3 V vs. RHE is

observed. The steady cathodic scan could be a result of a mixture of O_2/*OOH adsorption and subsequent H_2O_2 desorption at potentials of $E > E_{redox}$ where ORR is more active.

Summarizing all of the results above, we propose the following mechanisms for the electrochemical cycling of Ni-HAB in Ar and O_2 and the ORR processes (Scheme 1). In Ar-saturated electrolyte, Ni-HAB follows a simple cycling behavior that modifies the oxidation state and coordination of the Ni site (Scheme 1a), consequently causing cycling between Ni(II) at $E < E_{redox}$ and Ni(III) at $E > E_{redox}$ as a consequence of delocalized charge through the Ni-organic linker complex. The increased oxidation state of Ni relative to the sample measured in air suggests some intrinsic interaction with oxygen, further supported by the dependence of O_2 during the synthesis of Ni-HAB (Figure S1) and the LCA (Figure S22). In O_2-rich environments, oxygenates initially adsorb to the Ni site (Scheme 1b, i), but are not preferentially further reduced. Subsequently, *OOH adsorbates fill the pores as reductive overpotential is applied (Scheme 1b, ii), which then act as typical electrocatalytic $2e^-$ ORR active sites when $E > E_{redox}$ to produce H_2O_2 as shown in the upper loop of Scheme 1b. When the potential is scanned anodically to $E < E_{redox}$, the *OOH adsorbates undergo a two proton two electron reduction process to produce H_2O_2 and O_2 readsorbs to sites that are vacated by H_2O_2 release (without subsequent readsorption) while the linker becomes reduced (Scheme 1b, iii), allowing the catalyst to return to the approximate original mass of the starting state. Subsequently at even greater cathodic potentials $E << E_{redox}$, this O_2 can become further reduced to *OOH and become strongly adsorbed on the Ni site (Scheme 1b, iv), before the surface is "cleaned" to release H_2O_2 as it is scanned back anodically to $E > E_{redox}$ to its original resting state, where O_2 can readsorb to start the next cycle (Scheme 1b, v). In principle, this discharge-release process is similar to the previously demonstrated capture of ethylene by a redox active MOF.[59] To further experimentally validate this hypothesis, we conducted a

"poisoning experiment" using potassium thiocyanate (KSCN), which strongly binds to and serves to block off the Ni sites. But no change in ORR activity for Ni-HAB in the H_2O_2 selective region ($E > E_{redox}$) was observed (Figure S27), further confirming that Ni does not directly contribute to the ORR activity in this potential range.

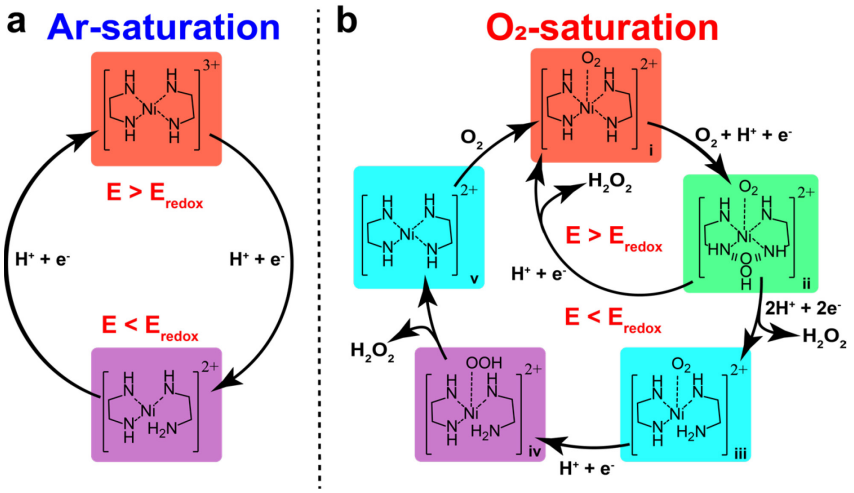

Scheme 1. Proposed redox and catalytic mechanisms during potential cycling on Ni-HAB in a) Ar and b) O_2 saturated environments. At lower overpotential ($E > E_{redox}$), $2e^-$ ORR is catalyzed by the organic linker (panel b upper loop); at higher overpotential ($E < E_{redox}$), $2e^-$ ORR is catalyzed by a combination of the linker and the Ni sites (panel b lower loop).

Bulk Electrochemical Synthesis of H_2O_2 in Neutral Media. To demonstrate the viability of Ni-HAB as a practical $2e^-$ ORR catalyst, we conducted bulk electrosynthesis of H_2O_2 on a ~1 cm^2 Ni-HAB/CFP electrode (Figure S28) in O_2-saturated 0.5 M NaPi buffer solution (pH = 6.64, 5 mL initial volume) with the potential of the electrode held constant in an H-cell. Aliquots of electrolyte (50 µL or 25 µL) were periodically taken out from the working chamber and added to portions of $Ce(SO_4)_2$ that were measured spectroscopically by UV-Vis (Figure S29) to determine the concentration of H_2O_2 (see Supporting Information for details). The electrode was operated for 90

minutes at 0.6 V, 0.5 V, and then 0.4 V vs. RHE in fresh solutions (Figure 5a). In accordance with the RRDE measurements, as the electrolysis potential approached E_{redox}, the total H_2O_2 concentration reached a peak of 662 ppm at 0.4 V vs. RHE (Figure 5b), which corresponds to a peak H_2O_2 yield of 86.2 µmol (Figure 5c).

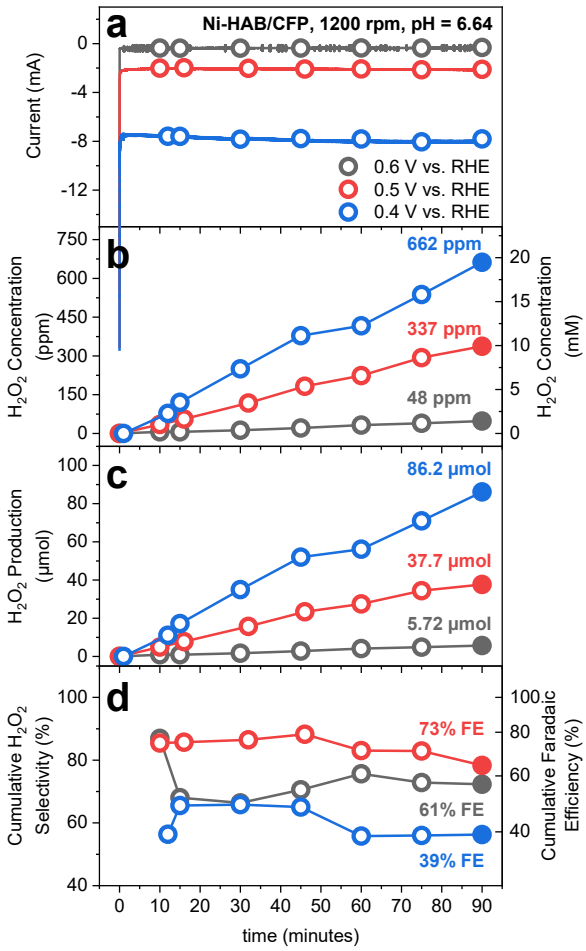

Figure 5. Bulk electrosynthesis and chemical detection of H_2O_2 produced on Ni-HAB/CFP. a) Chronoamperometry curve of Ni-HAB/CFP at 0.6 V, 0.5 V, and 0.4 V vs. RHE in O_2-saturated 0.05 M NaPi buffer solution (pH = 6.64). b) Cumulative H_2O_2 concentration, c) cumulative H_2O_2 yield, and d) cumulative H_2O_2 selectivity and Faradaic efficiency during bulk electrolyses.

Consistent with the RRDE measurements, the bulk electrolysis performed at 0.5 V vs. RHE showed the highest selectivity, with a Faradaic efficiency of 73% at the end of the measurement (Figure 5d). Further increasing the overpotential to 0.4 V vs. RHE results in a 39% Faradaic efficiency at the end of the measurement. The higher and more consistent selectivity over longer timescales at 0.5 V or 0.6 V vs. RHE are due to the minimization of linker charging during the measurement, as additionally evidenced by the much lower observed currents compared to that at 0.4 V vs. RHE (Figure 5a). Thus, electrolysis at 0.4 V vs. RHE results in faster accumulation of H_2O_2, but at the cost of lower Faradaic efficiency. Longer operation at lower potentials could lead to a more ideal combination of Faradaic efficiency and total H_2O_2 accumulation. High concentrations (up to 213 ppm) of H_2O_2 could also be accumulated at 0.6 V vs. RHE over ~6 hours, with fairly constant high selectivity over the entire measurement (Figure S30). The full results of these electroylsis measurements are shown in Table S21, and compared to various other examples of catalysts measured in neutral electrolyte in Table S22. To ensure that the H_2O_2 originated entirely from the Ni-HAB catalyst, we conducted an electrolysis on CFP with no catalyst loading at 0.4 V vs. RHE (Figure S31) and observed very low current, confirming the negligible contribution from the CFP substrate. Additionally, structural characterization after treatment tests of Ni-HAB with pure H_2O_2 solutions (Figure S32) suggest that Ni-HAB remains crystalline and does not become significantly oxidized after exposure to up to 1 wt.% of H_2O_2, suggesting that Ni-HAB could remain stable in optimized device architectures that allow for accumulation of reasonably high concentrations of H_2O_2.

CV scans before the electrolysis at 0.6 V vs. RHE (Figure S33) revealed only a small difference between the current at 0.6 V, 0.5 V, and 0.4 V before and after electrolysis, indicating minimal further reduction of H_2O_2 on Ni-HAB at these potentials, and thus confirming that the

potential choice is appropriate. Meanwhile, there are large increases in the current as the redox potential is approached (in excess of the current density measured on the pristine electrode) suggesting potentials ≤ E_{redox} (or approaching E_{redox}) would additionally interfere with the ORR via further reduction of H_2O_2 to H_2O, as suggested by RRDE and the operando XAS. Operating the electrolysis at 0.6 or 0.5 V vs. RHE likely minimizes the shift of charge density from the linker active site to Ni, which is indirectly observed through the reduction of the Ni in the Ar-saturated XANES measurements, and can cause overbound oxygenate adsorbates and decreases the selectivity for H_2O_2 production. However, the reduced catalyst can be easily "reset" by exposure to ambient air outside of the O_2-saturated electrolyte through the linker-mediated self-discharge process.

CONCLUSIONS

We show that 2D-MOF Ni_3HAB_2 is an active and selective catalyst for $2e^-$ ORR in neutral solution, but its actual operating state and active site are potential and environment dependent. RRDE electrochemical measurements initially suggested possible interference between the redox reaction of the HAB linker and the catalyst operation. Detailed operando XAS studies reveal that the redox of HAB linkers at a potential of E_{redox} dynamically alters the Ni oxidation state, and both Ni and the HAB linker have interactions with oxygenate adsorbates that are dependent on this evolving potential-dependent redox speciation. We hypothesize that a simpler $2e^-$ ORR mechanism proceeds via the reduction of *OOH adsorbed on the HAB linker when $E > E_{redox}$, while a complex Ni-mediated linker discharge and electrocatalytic interaction occurs at $E < E_{redox}$, the exact mechanism of which further is elucidated by post-operation EXAFS and RRDE results in addition to EQCM. Guided by these mechanistic understandings, by choosing an operating potential of 0.5 V vs. RHE to minimize the effects of shifting oxidation states of the catalyst during the bulk

electrolysis, a buildup of 337 ppm of H_2O_2 in 90 minutes with a final Faradaic efficiency of 73%, or up to 662 ppm with a consequent lower Faradaic efficiency of 39% at 0.4 V vs. RHE can be achieved using a Ni-HAB/CFP electrode in a buffered neutral solution. These findings could stimulate the development of MOF or SAC catalysts with similar properties to Ni_3HAB_2, but with slower or suppressed linker redox features that could lead to further improved $2e^-$ ORR catalysts that are active and selective across a larger potential range. Future developments in operando soft XAS could enable more in-depth and definitve understanding of the evolution of the surface-senistive electronic and structural environments on MOF or SAC catalysts with similar redox-ORR interactions and further stimulate systematic design of linkers that show modified redox potentials. This study not only establishes an efficient 2D MOF electrocatalyst for $2e^-$ ORR in neutral solutions but also provide a clear mechanistic understanding to enable the design of even better MOF electrocatalysts in the future.

AUTHOR INFORMATION

Corresponding Author

*jin@chem.wisc.edu

ORCID: 0000-0001-8693-7010

The authors declare no competing financial interests.

ASSOCIATED CONTENT

Supporting Information.

The Supporting Information is available free of charge on the ACS Publications website.

Experimental methods, additional figures, and tables on materials characterization, electrochemical measurements, and full details of the spectroscopic fittings.

ACKNOWLEDGMENTS

This work is supported by the National Science Foundation (NSF) Grant CHE-1955074. This research used resources of the Advanced Photon Source (APS), a U.S. Department of Energy (DOE) Office of Science User Facility operated for the DOE Office of Science by Argonne National Laboratory under Contract No. DE-AC02-06CH11357. MRCAT operations are supported by the Department of Energy and the MRCAT member institutions. The authors gratefully acknowledge use of facilities and instrumentation at the UW-Madison Wisconsin Centers for Nanoscale Technology partially supported by the NSF through the Materials Research Science and Engineering Center (DMR-1720415). The authors thank David S. Roberts for assistance in collecting the TEM images, Steve Myers for assistance in designing and constructing the electrochemical cell for operando measurements, and Dr. Rob McClain for providing training and access to the instrumentation for the BET and UV-Vis measurements.

REFERENCES

(1) Yang, S.; Verdaguer-Casadevall, A.; Arnarson, L.; Silvioli, L.; Čolić, V.; Frydendal, R.; Rossmeisl, J.; Chorkendorff, I.; Stephens, I. E. L. Toward the Decentralized Electrochemical Production of H_2O_2: A Focus on the Catalysis. *ACS Catal.* **2018**, *8*, 4064–4081. https://doi.org/10.1021/acscatal.8b00217.

(2) Jung, E.; Shin, H.; Hooch Antink, W.; Sung, Y. E.; Hyeon, T. Recent Advances in Electrochemical Oxygen Reduction to H_2O_2: Catalyst and Cell Design. *ACS Energy Lett.* **2020**, *5*, 1881–1892. https://doi.org/10.1021/acsenergylett.0c00812.

(3) Wang, Y.; Waterhouse, G. I. N.; Shang, L.; Zhang, T. Electrocatalytic Oxygen Reduction to Hydrogen Peroxide: From Homogeneous to Heterogeneous Electrocatalysis. *Adv. Energy Mater.* **2021**, *11*, 2003323. https://doi.org/10.1002/aenm.202003323.

(4) Zhou, W.; Meng, X.; Gao, J.; Alshawabkeh, A. N. Hydrogen Peroxide Generation from O_2

Electroreduction for Environmental Remediation: A State-of-the-Art Review. *Chemosphere* **2019**, *225*, 588–607. https://doi.org/10.1016/j.chemosphere.2019.03.042.

(5) Wang, N.; Ma, S.; Zuo, P.; Duan, J.; Hou, B. Recent Progress of Electrochemical Production of Hydrogen Peroxide by Two-Electron Oxygen Reduction Reaction. *Adv. Sci.* **2021**, *8*, 2100076. https://doi.org/10.1002/advs.202100076.

(6) Qiang, Z.; Chang, J.-H.; Huang, C.-P. Electrochemical Generation of Hydrogen Peroxide from Dissolved Oxygen in Acidic Solutions. *Water Res.* **2002**, *36*, 85–94. https://doi.org/10.1016/S0043-1354(01)00235-4.

(7) Xia, C.; Xia, Y.; Zhu, P.; Fan, L.; Wang, H. Direct Electrosynthesis of Pure Aqueous H_2O_2 Solutions up to 20% by Weight Using a Solid Electrolyte. *Science* **2019**, *366*, 226–231. https://doi.org/10.1126/science.aay1844.

(8) Li, H.; Wen, P.; Itanze, D. S.; Hood, Z. D.; Adhikari, S.; Lu, C.; Ma, X.; Dun, C.; Jiang, L.; Carroll, D. L.; Qiu, Y.; Geyer, S. M. Scalable Neutral H_2O_2 Electrosynthesis by Platinum Diphosphide Nanocrystals by Regulating Oxygen Reduction Reaction Pathways. *Nat. Commun.* **2020**, *11*, 3928. https://doi.org/10.1038/s41467-020-17584-9.

(9) Sun, Y.; Silvioli, L.; Sahraie, N. R.; Ju, W.; Li, J.; Zitolo, A.; Li, S.; Bagger, A.; Arnarson, L.; Wang, X.; Moeller, T.; Bernsmeier, D.; Rossmeisl, J.; Jaouen, F.; Strasser, P. Activity–Selectivity Trends in the Electrochemical Production of Hydrogen Peroxide over Single-Site Metal–Nitrogen–Carbon Catalysts. *J. Am. Chem. Soc.* **2019**, *141*, 12372–12381. https://doi.org/10.1021/jacs.9b05576.

(10) Sun, Y.; Sinev, I.; Ju, W.; Bergmann, A.; Dresp, S.; Kühl, S.; Spöri, C.; Schmies, H.; Wang, H.; Bernsmeier, D.; Paul, B.; Schmack, R.; Kraehnert, R.; Roldan Cuenya, B.; Strasser, P. Efficient Electrochemical Hydrogen Peroxide Production from Molecular Oxygen on Nitrogen-Doped Mesoporous Carbon Catalysts. *ACS Catal.* **2018**, *8*, 2844–2856. https://doi.org/10.1021/acscatal.7b03464.

(11) Jung, E.; Shin, H.; Lee, B.-H.; Efremov, V.; Lee, S.; Lee, H. S.; Kim, J.; Hooch Antink, W.; Park, S.; Lee, K.-S.; Cho, S.-P.; Yoo, J. S.; Sung, Y.-E.; Hyeon, T. Atomic-Level Tuning of Co–N–C Catalyst for High-Performance Electrochemical H_2O_2 Production. *Nat. Mater.* **2020**, *19*, 436–442. https://doi.org/10.1038/s41563-019-0571-5.

(12) Gao, J.; Yang, H. bin; Huang, X.; Hung, S.-F.; Cai, W.; Jia, C.; Miao, S.; Chen, H. M.; Yang, X.; Huang, Y.; Zhang, T.; Liu, B. Enabling Direct H_2O_2 Production in Acidic Media through Rational Design of Transition Metal Single Atom Catalyst. *Chem* **2020**, *6*, 658–674. https://doi.org/10.1016/j.chempr.2019.12.008.

(13) Jiang, K.; Back, S.; Akey, A. J.; Xia, C.; Hu, Y.; Liang, W.; Schaak, D.; Stavitski, E.; Nørskov, J. K.; Siahrostami, S.; Wang, H. Highly Selective Oxygen Reduction to Hydrogen Peroxide on Transition Metal Single Atom Coordination. *Nat. Commun.* **2019**, *10*, 3997. https://doi.org/10.1038/s41467-019-11992-2.

(14) Liu, C.; Li, H.; Liu, F.; Chen, J.; Yu, Z.; Yuan, Z.; Wang, C.; Zheng, H.; Henkelman, G.; Wei, L.; Chen, Y. Intrinsic Activity of Metal Centers in Metal-Nitrogen-Carbon Single-

Atom Catalysts for Hydrogen Peroxide Synthesis. *J. Am. Chem. Soc.* **2020**, *142*, 21861–21871. https://doi.org/10.1021/jacs.0c10636.

(15) Tang, C.; Chen, L.; Li, H.; Li, L.; Jiao, Y.; Zheng, Y.; Xu, H.; Davey, K.; Qiao, S. Tailoring Acidic Oxygen Reduction Selectivity on Single-Atom Catalysts via Modification of First and Second Coordination Spheres. *J. Am. Chem. Soc.* **2021**, *143*, 7819–7827. https://doi.org/10.1021/jacs.1c03135.

(16) Ross, R. D.; Sheng, H.; Parihar, A.; Huang, J.; Jin, S. Compositionally Tuned Trimetallic Thiospinel Catalysts for Enhanced Electrosynthesis of Hydrogen Peroxide and Built-In Hydroxyl Radical Generation. *ACS Catal.* **2021**, *11*, 12643–12650. https://doi.org/10.1021/acscatal.1c03349.

(17) Sheng, H.; Hermes, E. D.; Yang, X.; Ying, D.; Janes, A. N.; Li, W.; Schmidt, J. R.; Jin, S. Electrocatalytic Production of H_2O_2 by Selective Oxygen Reduction Using Earth-Abundant Cobalt Pyrite (CoS_2). *ACS Catal.* **2019**, *9*, 8433–8442. https://doi.org/10.1021/acscatal.9b02546.

(18) Liang, J.; Wang, Y.; Liu, Q.; Luo, Y.; Li, T.; Zhao, H.; Lu, S.; Zhang, F.; Asiri, A. M.; Liu, F.; Ma, D.; Sun, X. Electrocatalytic Hydrogen Peroxide Production in Acidic Media Enabled by NiS_2 Nanosheets. *J. Mater. Chem. A* **2021**, *9*, 6117–6122. https://doi.org/10.1039/d0ta12008a.

(19) Sheng, H.; Janes, A. N.; Ross, R. D.; Kaiman, D.; Huang, J.; Song, B.; Schmidt, J. R.; Jin, S. Stable and Selective Electrosynthesis of Hydrogen Peroxide and the Electro-Fenton Process on $CoSe_2$ Polymorph Catalysts. *Energy Environ. Sci.* **2020**, *13*, 4189–4203. https://doi.org/10.1039/d0ee01925a.

(20) Zhang, X. L.; Su, X.; Zheng, Y. R.; Hu, S. J.; Shi, L.; Gao, F. Y.; Yang, P. P.; Niu, Z. Z.; Wu, Z. Z.; Qin, S.; Wu, R.; Duan, Y.; Gu, C.; Zheng, X. S.; Zhu, J. F.; Gao, M. R. Strongly Coupled Cobalt Diselenide Monolayers for Selective Electrocatalytic Oxygen Reduction to H_2O_2 under Acidic Conditions. *Angew. Chem. Int. Ed* **2021**, *60*, 2–11. https://doi.org/10.1002/anie.202111075.

(21) Jin, S. How to Effectively Utilize MOFs for Electrocatalysis. *ACS Energy Lett.* **2019**, *4*, 1443–1445. https://doi.org/10.1021/acsenergylett.9b01134.

(22) Dhakshinamoorthy, A.; Asiri, A. M.; Garcia, H. 2D Metal–Organic Frameworks as Multifunctional Materials in Heterogeneous Catalysis and Electro/Photocatalysis. *Adv. Mater.* **2019**, *31*, 1900617. https://doi.org/10.1002/adma.201900617.

(23) Bavykina, A.; Kolobov, N.; Khan, I. S.; Bau, J. A.; Ramirez, A.; Gascon, J. Metal–Organic Frameworks in Heterogeneous Catalysis: Recent Progress, New Trends, and Future Perspectives. *Chem. Rev.* **2020**, *120*, 8468–8535. https://doi.org/10.1021/acs.chemrev.9b00685.

(24) Jiang, H.; Alezi, D.; Eddaoudi, M. A Reticular Chemistry Guide for the Design of Periodic Solids. *Nat. Rev. Mater.* **2021**, *6*, 466–487. https://doi.org/10.1038/s41578-021-00287-y.

(25) Lee, S. H.; Kim, J.; Chung, D. Y.; Yoo, J. M.; Lee, H. S.; Kim, M. J.; Mun, B. S.; Kwon, S. G.; Sung, Y. E.; Hyeon, T. Design Principle of Fe-N-C Electrocatalysts: How to Optimize Multimodal Porous Structures? *J. Am. Chem. Soc.* **2019**, *141*, 2035–2045. https://doi.org/10.1021/jacs.8b11129.

(26) Ko, M.; Mendecki, L.; Mirica, K. A. Conductive Two-Dimensional Metal–Organic Frameworks as Multifunctional Materials. *Chem. Commun.* **2018**, *54*, 7873–7891. https://doi.org/10.1039/C8CC02871K.

(27) Xie, L. S.; Skorupskii, G.; Dincă, M. Electrically Conductive Metal-Organic Frameworks. *Chem. Rev.* **2020**, *120*, 8536–8580. https://doi.org/10.1021/acs.chemrev.9b00766.

(28) Sheberla, D.; Sun, L.; Blood-Forsythe, M. A.; Er, S.; Wade, C. R.; Brozek, C. K.; Aspuru-Guzik, A.; Dincă, M. High Electrical Conductivity in Ni_3(2,3,6,7,10,11-Hexaiminotriphenylene)$_2$, a Semiconducting Metal-Organic Graphene Analogue. *J. Am. Chem. Soc.* **2014**, *136*, 8859–8862. https://doi.org/10.1021/ja502765n.

(29) Lahiri, N.; Lotfizadeh, N.; Tsuchikawa, R.; Deshpande, V. V.; Louie, J. Hexaaminobenzene as a Building Block for a Family of 2D Coordination Polymers. *J. Am. Chem. Soc.* **2017**, *139*, 19–22. https://doi.org/10.1021/jacs.6b09889.

(30) Park, J.; Lee, M.; Feng, D.; Huang, Z.; Hinckley, A. C.; Yakovenko, A.; Zou, X.; Cui, Y.; Bao, Z. Stabilization of Hexaaminobenzene in a 2D Conductive Metal–Organic Framework for High Power Sodium Storage. *J. Am. Chem. Soc.* **2018**, *140*, 10315–10323. https://doi.org/10.1021/jacs.8b06020.

(31) Hinckley, A. C.; Park, J.; Gomes, J.; Carlson, E.; Bao, Z. Air-Stability and Carrier Type in Conductive M_3(Hexaaminobenzene)$_2$,(M = Co, Ni, Cu). *J. Am. Chem. Soc.* **2020**, *142*, 11123–11130. https://doi.org/10.1021/jacs.0c03500.

(32) Feng, D.; Lei, T.; Lukatskaya, M. R.; Park, J.; Huang, Z.; Lee, M.; Shaw, L.; Chen, S.; Yakovenko, A. A.; Kulkarni, A.; Xiao, J.; Fredrickson, K.; Tok, J. B.; Zou, X.; Cui, Y.; Bao, Z. Robust and Conductive Two-Dimensional Metal−organic Frameworks with Exceptionally High Volumetric and Areal Capacitance. *Nat. Energy* **2018**, *3*, 30–36. https://doi.org/10.1038/s41560-017-0044-5.

(33) Gao, G.; Waclawik, E. R.; Du, A. Computational Screening of Two-Dimensional Coordination Polymers as Efficient Catalysts for Oxygen Evolution and Reduction Reaction. *J. Catal.* **2017**, *352*, 579–585. https://doi.org/10.1016/j.jcat.2017.06.032.

(34) Wang, J.; Fan, Y.; Qi, S.; Li, W.; Zhao, M. Bifunctional HER/OER or OER/ORR Catalytic Activity of Two-Dimensional TM_3(HITP)$_2$ with TM = Fe–Zn. *J. Phys. Chem. C* **2020**, *124*, 9350–9359. https://doi.org/10.1021/acs.jpcc.0c01143.

(35) Miner, E. M.; Gul, S.; Ricke, N. D.; Pastor, E.; Yano, J.; Yachandra, V. K.; Van Voorhis, T.; Dincă, M. Mechanistic Evidence for Ligand-Centered Electrocatalytic Oxygen Reduction with the Conductive MOF Ni_3(Hexaiminotriphenylene)$_2$. *ACS Catal.* **2017**, *7*, 7726–7731. https://doi.org/10.1021/acscatal.7b02647.

(36) Miner, E. M.; Fukushima, T.; Sheberla, D.; Sun, L.; Surendranath, Y.; Dincə, M. Electrochemical Oxygen Reduction Catalysed by Ni_3(Hexaiminotriphenylene)$_2$. *Nat. Commun.* **2016**, *7*, 10942. https://doi.org/10.1038/ncomms10942.

(37) Park, J.; Chen, Z.; Flores, R. A.; Wallnerström, G.; Kulkarni, A.; Nørskov, J. K.; Jaramillo, T. F.; Bao, Z. Two-Dimensional Conductive Ni-HAB as a Catalyst for the Electrochemical Oxygen Reduction Reaction. *ACS Appl. Mater. Interfaces* **2020**, *12*, 39074–39081. https://doi.org/10.1021/acsami.0c09323.

(38) Miner, E. M.; Wang, L.; Dincă, M. Modular O_2 Electroreduction Activity in Triphenylene-Based Metal-Organic Frameworks. *Chem. Sci.* **2018**, *9*, 6286–6291. https://doi.org/10.1039/c8sc02049c.

(39) Ni, Y.; Lin, L.; Shang, Y.; Luo, L.; Wang, L.; Lu, Y.; Li, Y.; Yan, Z.; Zhang, K.; Cheng, F.; Chen, J. Regulating Electrocatalytic Oxygen Reduction Activity of a Metal Coordination Polymer via d–π Conjugation. *Angew. Chem. Int. Ed* **2021**, *60*, 16937–16941. https://doi.org/10.1002/anie.202104494.

(40) Lian, Y.; Yang, W.; Zhang, C.; Sun, H.; Deng, Z.; Xu, W.; Song, L.; Ouyang, Z.; Wang, Z.; Guo, J.; Peng, Y. Unpaired 3d Electrons on Atomically Dispersed Cobalt Centres in Coordination Polymers Regulate Both Oxygen Reduction Reaction (ORR) Activity and Selectivity for Use in Zinc–Air Batteries. *Angew. Chem. Int. Ed* **2020**, *59*, 286–294. https://doi.org/10.1002/anie.201910879.

(41) Lukatskaya, M. R.; Feng, D.; Bak, S. M.; To, J. W. F.; Yang, X. Q.; Cui, Y.; Feldblyum, J. I.; Bao, Z. Understanding the Mechanism of High Capacitance in Nickel Hexaaminobenzene-Based Conductive Metal-Organic Frameworks in Aqueous Electrolytes. *ACS Nano* **2020**, *14*, 15919–15925. https://doi.org/10.1021/acsnano.0c07292.

(42) Rosen, A. S.; Mian, M. R.; Islamoglu, T.; Chen, H.; Farha, O. K.; Notestein, J. M.; Snurr, R. Q. Tuning the Redox Activity of Metal–Organic Frameworks for Enhanced, Selective O_2 Binding: Design Rules and Ambient Temperature O_2 Chemisorption in a Cobalt–Triazolate Framework. *J. Am. Chem. Soc.* **2020**, *142*, 4317–4328. https://doi.org/10.1021/jacs.9b12401.

(43) Lien, H.-T.; Chang, S.-T.; Chen, P.-T.; Wong, D. P.; Chang, Y.-C.; Lu, Y.-R.; Dong, C.-L.; Wang, C.-H.; Chen, K.-H.; Chen, L.-C. Probing the Active Site in Single-Atom Oxygen Reduction Catalysts via Operando X-Ray and Electrochemical Spectroscopy. *Nat. Commun.* **2020**, *11*, 4233. https://doi.org/10.1038/s41467-020-17975-y.

(44) Ramaker, D. E.; Korovina, A.; Croze, V.; Melke, J.; Roth, C. Following ORR Intermediates Adsorbed on a Pt Cathode Catalyst during Break-in of a PEM Fuel Cell by in Operando X-Ray Absorption Spectroscopy. *Phys. Chem. Chem. Phys.* **2014**, *16*, 13645–13653. https://doi.org/10.1039/C4CP00192C.

(45) Timoshenko, J.; Roldan Cuenya, B. In Situ/Operando Electrocatalyst Characterization by X-Ray Absorption Spectroscopy. *Chem. Rev.* **2021**, *121*, 882–961. https://doi.org/10.1021/acs.chemrev.0c00396.

(46) Zhu, Y.; Wang, J.; Chu, H.; Chu, Y. C.; Chen, H. M. In Situ/Operando Studies for Designing Next-Generation Electrocatalysts. *ACS Energy Lett.* **2020**, *5*, 1281–1291. https://doi.org/10.1021/acsenergylett.0c00305.

(47) Phua, E. J. H.; Wu, K. H.; Wada, K.; Kusamoto, T.; Maeda, H.; Cao, J.; Sakamoto, R.; Masunaga, H.; Sasaki, S.; Mei, J. W.; Jiang, W.; Liu, F.; Nishihara, H. Oxidation-Promoted Interfacial Synthesis of Redox-Active Bis(Diimino)Nickel Nanosheet. *Chem. Lett.* **2018**, *47*, 126–129. https://doi.org/10.1246/cl.170928.

(48) Kropf, A. J.; Katsoudas, J.; Chattopadhyay, S.; Shibata, T.; Lang, E. A.; Zyryanov, V. N.; Ravel, B.; McIvor, K.; Kemner, K. M.; Scheckel, K. G.; Bare, S. R.; Terry, J.; Kelly, S. D.; Bunker, B. A.; Segre, C. U.; Garrett, R.; Gentle, I.; Nugent, K.; Wilkins, S. The New MRCAT (Sector 10) Bending Magnet Beamline at the Advanced Photon Source. In *AIP Conference Proceedings*; 2010; Vol. 1234, pp 299–302. https://doi.org/10.1063/1.3463194.

(49) Dou, J. H.; Sun, L.; Ge, Y.; Li, W.; Hendon, C. H.; Li, J.; Gul, S.; Yano, J.; Stach, E. A.; Dincă, M. Signature of Metallic Behavior in the Metal-Organic Frameworks M_3(Hexaiminobenzene)$_2$ (M = Ni, Cu). *J. Am. Chem. Soc.* **2017**, *139*, 13608–13611. https://doi.org/10.1021/jacs.7b07234.

(50) Zilbermann, I.; Maimon, E.; Cohen, H.; Meyerstein, D. Redox Chemistry of Nickel Complexes in Aqueous Solutions. *Chem. Rev.* **2005**, *105*, 2609–2626. https://doi.org/10.1021/cr030717f.

(51) Liu, M.; Li, Y.; Qi, Z.; Su, H.; Cheng, W.; Zhou, W.; Zhang, H.; Sun, X.; Zhang, X.; Xu, Y.; Jiang, Y.; Liu, Q.; Wei, S. Self-Nanocavity-Confined Halogen Anions Boosting the High Selectivity of the Two-Electron Oxygen Reduction Pathway over Ni-Based MOFs. *J. Phys. Chem. Lett.* **2021**, *12*, 8706–8712. https://doi.org/10.1021/acs.jpclett.1c01981.

(52) Li, X.; Tang, S.; Dou, S.; Fan, H. J.; Choksi, T. S.; Wang, X. Molecule Confined Isolated Metal Sites Enable the Electrocatalytic Synthesis of Hydrogen Peroxide. *Adv. Mater.* **2022**, *34*, 2104891. https://doi.org/10.1002/adma.202104891.

(53) Segre, C. U.; Leyarovska, N. E.; Chapman, L. D.; Lavender, W. M.; Plag, P. W.; King, A. S.; Kropf, A. J.; Bunker, B. A.; Kemner, K. M.; Dutta;, P.; Duran, R. S.; Kaduk, J. The MRCAT Insertion Device Beamline at the Advanced Photon Source. In *AIP Conference Proceedings*; Pianetta, P., Arthur, J., Brennan, S., Eds.; AIP: New York, 2000; Vol. 521, pp 419–422. https://doi.org/10.1063/1.1291825.

(54) Ottenwaelder, X.; Aukauloo, A.; Journaux, Y.; Carrasco, R.; Cano, J.; Cervera, B.; Castro, I.; Curreli, S.; Mu, M. C.; Rosell, A. L.; Soto, B.; Ruiz-garc, R. Synthesis, Structure, Spectroscopy and Redox Chemistry of Square-Planar Nickel(II) Complexes with Tetradentate o-Phenylenedioxamidates and Related Ligands. *Dalt. Trans.* **2005**, No. 15, 2516–2526.

(55) Keegan, B. C.; Ocampo, D.; Shearer, J. pH Dependent Reversible Formation of a Binuclear Ni2 Metal-Center within a Peptide Scaffold. *Inorganics* **2019**, *7*, 90. https://doi.org/10.3390/inorganics7070090.

(56) Cutsail III, G. E.; DeBeer, S. Challenges and Opportunities for Applications of Advanced X-Ray Spectroscopy in Catalysis Research. *ACS Catal.* **2022**, *12*, 5864–5886. https://doi.org/10.1021/acscatal.2c01016.

(57) Mansour, A. N.; Melendres, C. A. Analysis of X-Ray Absorption Spectra of Some Nickel Oxycompounds Using Theoretical Standards. *J. Phys. Chem. A* **1998**, *102*, 65–81. https://doi.org/10.1021/jp9619853.

(58) Görlin, M.; Chernev, P.; De Araújo, J. F.; Reier, T.; Dresp, S.; Paul, B.; Krähnert, R.; Dau, H.; Strasser, P. Oxygen Evolution Reaction Dynamics, Faradaic Charge Efficiency, and the Active Metal Redox States of Ni-Fe Oxide Water Splitting Electrocatalysts. *J. Am. Chem. Soc.* **2016**, *138*, 5603–5614. https://doi.org/10.1021/jacs.6b00332.

(59) Mendecki, L.; Ko, M.; Zhang, X.; Meng, Z.; Mirica, K. A. Porous Scaffolds for Electrochemically Controlled Reversible Capture and Release of Ethylene. *J. Am. Chem. Soc.* **2017**, *139*, 17229–17232. https://doi.org/10.1021/jacs.7b08102.

For Table of Contents Only